processes

MDPI

*Review*

# From Waste Biomass to Hard Carbon Anodes: Predicting the Relationship between Biomass Processing Parameters and Performance of Hard Carbons in Sodium-Ion Batteries

**Yanghao Jin [1], Ziyi Shi [1], Tong Han [1,*], Hanmin Yang [1], Habtom Desta Asfaw [2], Ritambhara Gond [2], Reza Younesi [2], Pär G. Jönsson [1] and Weihong Yang [1]**

[1] Department of Material Science and Engineering, KTH Royal Institute of Technology, 11428 Stockholm, Sweden
[2] Department of Chemistry—Ångström Laboratory, Uppsala University, Lägerhyddsvägen 1, P.O. Box 539, 75121 Uppsala, Sweden
* Correspondence: tongh@kth.se

**Abstract:** Sodium-ion batteries (SIBs) serve as the most promising next-generation commercial batteries besides lithium-ion batteries (LIBs). Hard carbon (HC) from renewable biomass resources is the most commonly used anode material in SIBs. In this contribution, we present a review of the latest progress in the conversion of waste biomass to HC materials, and highlight their application in SIBs. Specifically, the following topics are discussed in the review: (1) the mechanism of sodium-ion storage in HC, (2) the HC precursor's sources, (3) the processing methods and conditions of the HCs production, (4) the impact of the biomass types and carbonization temperature on the carbon structure, and (5) the effect of various carbon structures on electrochemical performance. Data from various publications have been analyzed to uncover the relationship between the processing conditions of biomass and the resulting structure of the final HC product, as well as its electrochemical performance. Our results indicate the existence of an ideal temperature range (around 1200 to 1400 °C) that enhances the formation of graphitic domains in the final HC anode and reduces the formation of open pores from the biomass precursor. This results in HC anodes with high storage capacity (>300 mAh/g) and high initial coulombic efficiency (ICE) (>80%).

**Keywords:** waste biomass; hard carbon; sodium ion batteries; sodium-ion storage; anode material



**Citation:** Jin, Y.; Shi, Z.; Han, T.; Yang, H.; Asfaw, H.D.; Gond, R.; Younesi, R.; Jönsson, P.G.; Yang, W. From Waste Biomass to Hard Carbon Anodes: Predicting the Relationship between Biomass Processing Parameters and Performance of Hard Carbons in Sodium-Ion Batteries. *Processes* **2023**, *11*, 764. https://doi.org/10.3390/pr11030764

Academic Editor: Wen-Tien Tsai

Received: 13 January 2023
Revised: 27 February 2023
Accepted: 2 March 2023
Published: 4 March 2023



## 1. Introduction

Batteries are widely applied in portable electronics, electric vehicles, and large-scale applications such as grid energy storage, and are recognized as being key elements in realizing a carbon-neutral world [1]. Lithium-ion batteries (LIBs) are widely recognized as the most attractive batteries due to their high energy density, long cycle life [2], stability, compact and lightweight design [3], less environmental effect [4], and broad range of applications [5]. With advancements in theoretical research and production technology, lithium-ion batteries (LIBs) have gained dominance in the commercial battery market due to improved system design and manufacturing [3]. However, limited lithium reserves and uneven geographical distribution are expected to impede the long-term growth of the LIB market and result in higher prices/kWh [6–8]. Hence, finding alternative commercial batteries to supplement LIBs is imperative.

Sodium-ion batteries (SIBs) are considered a potential alternative to the lithium-ion battery market, especially for large-scale energy storage applications [9], due to their physical and chemical similarities to lithium, as well as the cost-effectiveness and abundant availability of sodium resources, as shown in Table 1 [10–12]. The energy density of a battery is a critical factor in its performance and market viability. Currently, some companies have already released their commercial SIBs. Faradion has developed a SIB with a

160 Wh/kg energy density, rapid charging efficiency, and excellent low-temperature performance [13]. Natrium and CATL also produce SIBs with energy densities of 120 Wh/kg [14] and 160 Wh/kg [15], respectively. Despite progress in the development of SIBs, there remains a substantial gap between their energy density and that of commercial LIBs (330 Wh/kg from CATL [15]).

**Table 1.** Comparison of Li and Na [10–12].

| | Li | Na |
|---|---|---|
| Cation radius (nm) | 0.076 | 0.106 |
| Ionization energy (eV) | 5.39 | 5.14 |
| Electronegativity | 0.98 | 0.93 |
| Standard electrode potential (V) | −3.04 | −2.71 |
| Molar mass (g/mol) | 6.9 | 23.0 |
| The ratio in Earth's crust | 0.0065% | 2.83% |
| Price of metal (USD/t) [16] | ~42,000 | ~2325 |

The disparity is primarily due to differences in the materials used in the electrodes and the reaction mechanism during charging and discharging. For instance, while graphite is the typical anode material in conventional lithium-ion batteries (LIBs); attempts to use it in sodium-ion batteries (SIBs) have been hindered as sodium has a larger radius than lithium, making it difficult to form graphite intercalation compounds [17] with a theoretic capacity of 35 mAh/g [18]. The most commonly used cathode materials for SIBs are layered oxides, polyanionic compounds, and Prussian blue analogues. Among them, layered oxides (Natrium [14]) and Prussian blue analogues (CATL [15]) have been used commercially [19]. The options for suitable anode materials in SIBs are listed in Table 2. Depending on the sodium storage mechanism of the anode material, sodium ion battery anodes can be divided into three types: intercalated, alloying, and conversion, with the latter two having higher theoretical capacities [20]. However, both alloying and conversion materials experience significant volume expansion during the sodium storage process, leading to electrode inactivation [12]. As a result, these anode materials are not yet mature enough for commercial use in SIBs.

**Table 2.** Suitable anode materials in SIBs.

| Material | Storage Mechanism | Theoretical Capacity | Example | Reversible Capacity mAh/g | ICE % | Price USD/kg | Refs. |
|---|---|---|---|---|---|---|---|
| Hard carbon | Intercalation, adsorption, filling | - | Hard carbon from poplar wood | 330 | 88.3 | 1.5 | [21] |
| Alloying (Sn, Si, P) | Alloying reaction $M + Na^+ + xe^- \leftrightarrow NaxM$ | 300–750 | Sn@C | 493.6 | - | 30 (Sn powder) | [22,23] |
| Titanate | Insertion | 200 | $Na_2Ti_6O_{13}$/ $Na_2Ti_3O_7$ | 173.6 | 64.4 | 2400 ($Na_2Ti_3O_7$) | [24–27] |
| Transition metal oxide (CuO, $MoO_2$) | Conversion reaction $MO_x + 2xNa^+ + 2xe^- \leftrightarrow xNa_2O + M$ | 400–900 | $Fe_2O_3$ | 323 | 63 | 50 ($Fe_2O_3$) | [20,28] |

Hard carbon (HC) is the most widely used anode material in SIBs due to its superior electrochemical performance and cost-effectiveness. The properties of some of the current commercial hard carbons can be found in Table 3.

**Table 3.** Properties of commercial hard carbon materials.

| Company (Product Name) | D50 (μm) | SSA ($m^2/g$) | Tap Density ($g/cm^3$) | First Reversible Capacity (mAh/g) | ICE (%) | Ref. |
|---|---|---|---|---|---|---|
| BTR (BSHC-300) | 6.0 ± 1.5 | ≤5.0 | 0.8 ± 0.1 | 295 ± 5.0 | ≥88 | [29] |
| BTR (BSHC-260) | 6.0 ± 1.5 | ≤5.0 | 0.9 ± 0.1 | 260 ± 5.0 | ≥88 | [29] |
| BSG (NHC-330) | 9.25 | 3.58 | 0.77 | 332.5 | 90.5 | [30] |
| BSG (YHC-1) | 9.1 | 5.27 | 0.65 | 294.6 | 89.2 | [30] |
| JFE | - | 0.7–5.0 | 1.61(true density) | ≥350 | - | [31] |

The main source of HC is waste biomass, which is abundant and low-cost. Converting waste biomass into high-quality HCs promotes the value-add application of solid waste, increases resource efficiency, and supports a circular economy. However, the biomass precursors have a highly oxygenated, crosslinked, and disordered structure [32], resulting in an irregular HC structure that cannot be graphitized and makes it difficult to build a standard model. Since the 1950s, many research efforts have been made in order to establish models that can adequately describe the structures of HCs [33]. Nowadays, it is widely accepted that the basic structural units of HC are randomly oriented stacks of hexagonal carbon layers [34]. Their random orientation leads to the formation of nano-graphitic domains with certain graphene layers, which provide storage sites for sodium ions [33,35,36]. However, there is still no clear mechanism for sodium storage in HC [37], and this has limited the further development of HC anodes. To address this issue, the current study gives a review of renewable biomass-derived HC as SIBs anodes. The proposed sodium storage mechanism, the influence of the biomass precursors, biomass carbonization parameters, and the influence of HC structure on its electrochemical performance are presented. At last, the relationship between carbonization parameters and HC electrochemical is investigated.

## 2. Sodium Storage Mechanism in HCs

The main structures of HC are surface defects, graphitic domains, and nanopores [12]. The graphitic domains are mainly determined by the following three parameters: (1) the crystal thickness along the c-axis ($L_c$), (2) the crystal width along the a-axis ($L_a$), and (3) the d-spacing between graphene layers ($d_{002}$) [17]. The XRD results are generally used to calculate these three parameters [34]. The nanopores of HC are divided into open and closed pores. They can be characterized by the micropore volume (V) and specific surface area (SSA) evaluated by the BET analysis. Defects in HC include pores in the bulk, dangling bonds, $sp^3$-hybridized carbon bonds, and surface functional groups. Raman spectroscopy is widely used to detect the structure of carbon material. There are 2 main Raman bands for HC materials, namely the D peak between 1320 $cm^{-1}$ and 1365 $cm^{-1}$ and the G peak between 1520 $cm^{-1}$ and 1600 $cm^{-1}$. The intensity or integrated area ratios ($I_D/I_G$) represent a measure of material defects and disordered structures [38]. However, there are no suitable parameters to quantitatively analyze surface functional groups. The sodium storage mechanism in HCs has been continuously updated since the 'house of card' model proposed by Steve et al. [39]. So far, the following four main storage models have been suggested: (1) an intercalation–pore filling model, (2) an adsorption–intercalation model, (3) an adsorption–pore filling model, and (4) an adsorption–intercalation–pore filling model [11]. Although there is no definite storage model, all of these models include three types of sodium ion storage in HC, as shown in Figure 1: (1) $Na^+$ ions adsorb at the defect sites on the surface; (2) $Na^+$ ions intercalate into graphitic layers; and (3) $Na^+$ ions fill the nanopores [40]. Overall, it can be concluded that the sodium-ion storage mechanism is closely related to the HC structure. As a result, an optimized biomass carbonization process plays a key role in the synthesis of HCs with a higher sodium storage capacity.

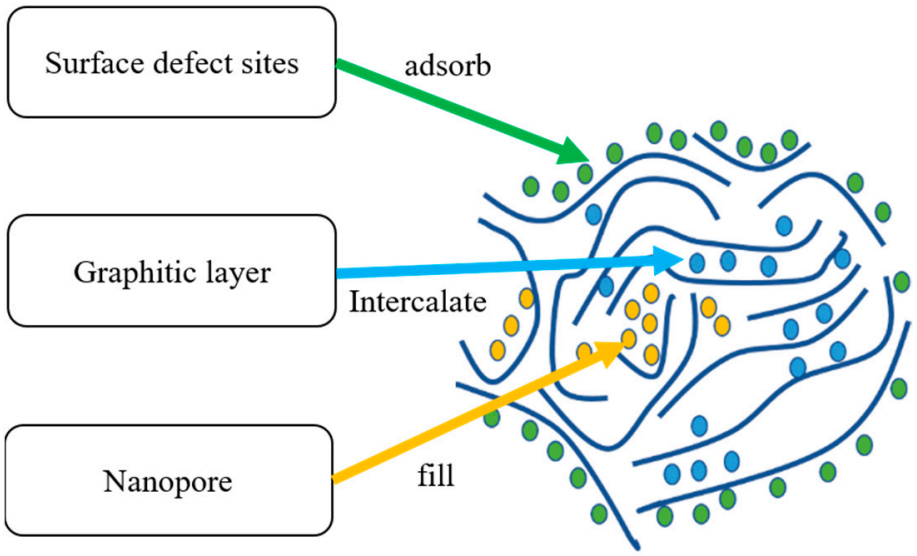


**Figure 1.** Mechanism of sodium ion storage in HC anodes [40].

## 3. HC Synthesis Process

### *3.1. Biomass Precursor*

A variety of biomass have been demonstrated to have the potential to become precursor materials for high-performance HC anodes. Compared to other HC precursors such as sugars and polymers, biomass precursors, with their wide range of sources, low cost, and environmental friendliness, are undoubtedly the most promising green HC precursor materials [41]. Owing to the diversity of biomass, the selection of suitable and reliable biomass raw materials depending on geographical conditions is crucial to the manufacturing of HC. In some studies, biomass-derived HCs show promising electrochemical performance, but a safe supply of biomass is hard to achieve.

#### 3.1.1. Origin Biomass

Origin biomass refers to raw biomass that is used directly in HC processing after harvesting. Seaweed [42], cotton [43], and trees [21] are all common origin biomass precursors. Origin biomass generally has a larger volume and a higher water content. These materials require more pre-treatment steps, such as grinding, drying, acid washing, and pyrolysis, to become suitable HC precursor materials [44]. In addition, these precursor materials have other well-established applications and are inherently valuable. This makes them inherently more expensive than other precursor materials. For example, timber prices in the market are at 430 USD/MBF [45], approximately equal to 260 USD/t. Therefore, the use of origin biomass as a precursor material for HC production would not only lead to a complex production process, but also increased production costs.

#### 3.1.2. Biomass By-Product

Biomass by-products are residues from the harvesting and processing of biomass and are mainly classified as industrial, forestry, and agricultural biomass by-products. Industrial biomass by-products are mainly derived from food or material processing. For example, residual sugarcane bagasse from the sugar industry, which is currently at 145 USD/t on the market [46]. Purna et.al obtained an HC anode with a capacity of 290 mAh/g and an ICE of 70% using sugarcane bagasse as precursor [47]. Lignin, the by-product from the paper industry, is also a widely used HC precursor material [48–50].

Forestry by-products are mostly residues from the tree harvesting process, such as sawdust, roots, and bark. Compared to wood, these forestry by-products have a similar composition, but are more affordable. Sawdust, for example, is currently priced at 50–200 USD/t [51] and has greater potential as a HC precursor material.

Agricultural by-products are mainly residues from the transformation of crops into products. These include straw, stems, and leaves left over from the harvesting process, as well as shells and peels from processing.

Agricultural by-products are a diverse and abundant source of material for biomass waste. The type and quantity of agricultural waste may vary depending on geographical conditions. For instance, Turkey produces an average of 0.5 Mt of hazelnuts annually, generating a substantial amount of waste from hazelnut shells [52]. The United States, being the top producer of corn with 383.9 Mt in 2021/2022 [53], has an extensive amount of waste in the form of corn straw and cobs. Meanwhile, China generates nearly 700 Mt of straw waste annually [54]. In the view of this, the selection of HC precursors needs to be made based on geographical considerations. Most of the agriculture waste biomass by-product has been reported to have potential as a HC precursor material. A summary of promising HC products derived from various agricultural by-products, including the processing conditions and their electrochemical performances, are listed in Table 4. It can be seen that the electrochemical performance of HCs is quite good, with a capacity higher than 350 mAh/g, and an ICE higher than 70%.

**Table 4.** Comparison of agricultural by-products-derived HC anodes for SIB.

| Precursor | Carbonization Temperature | Capacity mAh/g | ICE% | Capacity Retention | Ref. |
|---|---|---|---|---|---|
| Shaddock peel | 1200 °C | 430.5 (at 0.03 A/g) | 67.7 | 97.5% after 200 cycles | [55] |
| Pinecone | 1400 °C | 370 (at 0.03 A/g) | 85.4 | 90.3% after 120 cycles | [56] |
| Mangosteen shell | 1500 °C | 330 (at 0.02 A/g) | 83 | 98% after 100 cycles | [57] |
| Lotus Stem | 1400 °C | 351 (at 0.02 A/g) | 70 | 94% after 450 cycles | [58] |
| Waste cork | 1600 °C | 358 (at 0.03 A/g) | 81 | 71% after 2000 cycles | [59] |

#### 3.1.3. Biochar

Biochar, a product from biomass pyrolysis [60], is one of the commercial products that is of interest as a precursor to produce HCs. Advantages of the use of biochar include safe raw material supply and high carbon efficiency. Both types of biomass mentioned above can be used in biorefineries and obtain the corresponding biochar products [61]. Compared to biomass and biomass by-products, biochar has a higher carbon content (>70%) after the pyrolysis process (300–900 °C) [60]. This means that there is a higher yield of HC in the carbonization process and fewer by-products (syngas, bio-oil), which reduces the waste treatment process and improves the economics. Moreover, the two-step heat treatment process also increases the graphitization of the HC, thus improving the performance of the HC anode [62]. However, biochar, as an energy product, is currently more expensive on the market, at around 200–500 USD/t [63]. Meanwhile, after carbonization, the HC structure still retains a certain degree of similarity to the precursor [32]. Rios used biochar from four biomasses with similar C (50%), H (6%), and O (41%) contents as HC precursor materials. HC anodes with different electrochemical properties were obtained under the same conditions, including: pine (323.8 mAh/g, 85%), ash wood (280 mAh/g, 79%), miscanthus (274.9 mAh/g, 80%), and wheat straw (224.4 mAh/g, 65%) [64]. This means that the raw material for biochar still has a significant impact on HC performance.

The sources of all three types of biomass are limited by geographical as well as industrial conditions. Therefore, the primary consideration in the selection of HC precursor materials is the local condition. Secondly, the HC structure will vary depending on the main components of the biomass precursor material (cellulose, lignin, or hemicellulose). Therefore, the relationship between biomass type and HC structure must be explained in order to establish the basis for precursor material selection. Alternately, the material can be structurally modified to improve the HC structure. Finally, the economics of the production process should factor into the selection of HC precursor materials. Based on the biochar yield of the pyrolysis process and the carbon content in the biochar for these three types of biomass material [65–67], to obtain 1t HC requires around 6 t of origin biomass (timber [68],

water content is 20.9%; biocahr yield is 26%; carbon content in biochar is 81%; price around 1560 USD/t HC), 5.1 t of biomass by-product (sugarcane bagasse [69], water content is 6%; biocahr yield is 25.6%; carbon content in biochar is 81.5%; price around 739.3 USD/t HC), or 1t of biochar (carbon content above 99%; price around 500 USD/t HC (). Current prices for high purity HC (300 mAh/g, ICE > 80%) for SIBs and LIBs are around 1500 USD/t [70]. Controlling raw material costs and improving the performance of the final HC product are the keys to improving economics.

### *3.2. HC Production Process*

Figure 2 illustrates the process of converting biomass into HC. Origin biomass and biomass by-products can be transformed into biochar through a drying, grinding, and pyrolysis process. Additionally, these three types of biomass can also be directly converted into HC through high temperature carbonization at temperatures between 900 and 2000 °C for a duration of 0.5 to 6 h with a certain heating rate. Figure 3 shows that during this process, the biomass transforms into HC and small gas molecules precipitate out. The carbonization process involves simultaneous dehydrogenation, condensation, hydrogen transfer, and isomerization [33]. The final HC retains a non-graphitizable structure similar to the precursor material due to the highly oxygenated, crosslinked, and disordered structure of the precursor.

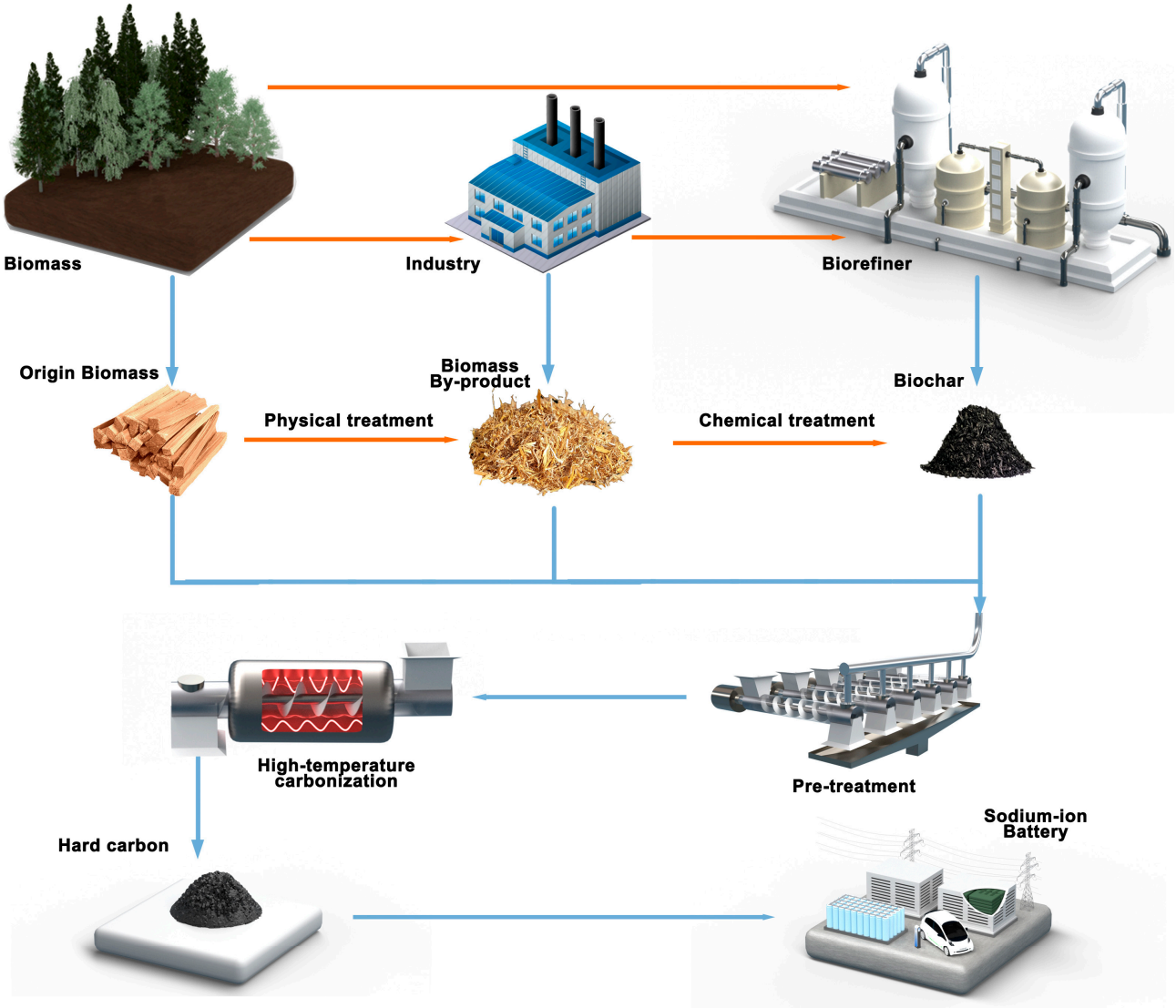


**Figure 2.** Processes involved in the production of hard carbon from biomass.

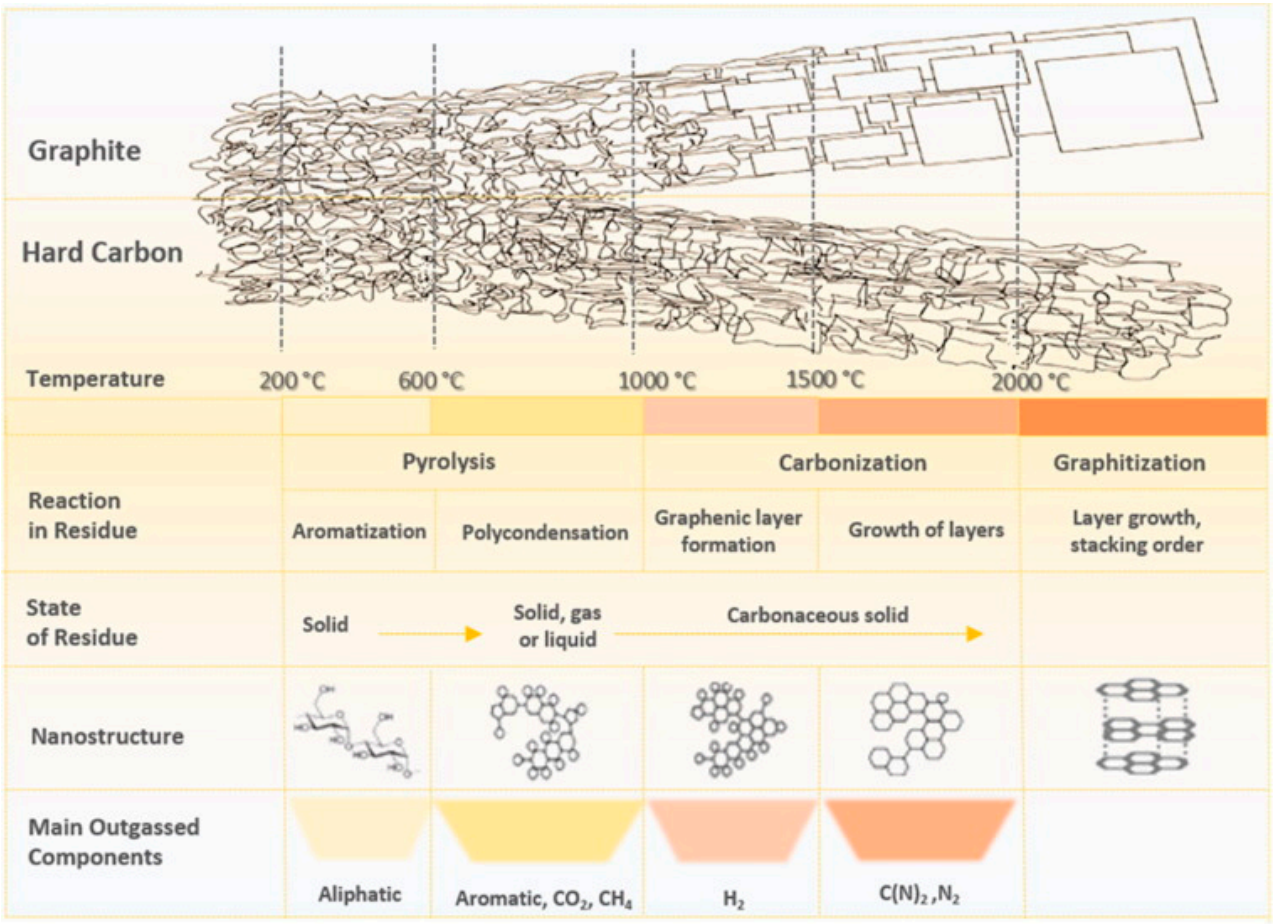


**Figure 3.** Hard-carbon formation scheme as a function of temperature [33] (Published in Materials Today, Volume 23, 2019,Dou (s), Hard carbons for sodium-ion batteries: Structure, analysis, sustainability, and electrochemistry, Pages 87–104, Copyright Elsevier (2023)).

Apart from the major carbonization process, an extra pre-treatment and post-treatment may also be included to improve the precursor structure, HC electrochemical performance, and economic process [32]. Specifically, these additional treatments include: acid wash for high ash content precursor [71]; activation to alter porosity [71]; heteroatom-doping for improving the surface chemistry of HC [72,73]; pre-sodiation to improve ICE and long-term cycling performance of the HC anode [74]; and catalytic graphitization to reduce the temperature requirement, and thus increase the economic process [75]. In the majority of studies, a direct carbonization of biomass by-product precursors is conducted without pre-/post-treatment. Therefore, the current review does not focus on the influence of the pre-/post-treatment.

## 4. Influence of Biomass Processing Parameter on the HC Structure

### *4.1. Influence of Biomass Precursor*

Biomass has vast sources and wide variations [76]. Lignin, cellulose, and hemicellulose are the main components of biomass [77]. The proportions of the three components of biomass vary considerably between biomass species. Even biomass originating from different regions of the same plant might differ in composition and structure [77]. As a result, the structure and properties of HCs are different [32]. Figure 4 gives a more specific summary of the HC structure parameters ($I_D/I_G$, SSA, $d_{002}$) derived from the different biomass species under the same carbonization condition: 1200 °C for 2 h [56–59,78–83]. The different colored dots represent different biomasses. It can be seen that the properties of hard carbon derived from different biomass species can greatly vary even under the same

carbonization conditions. For instance, the hard carbon derived from Ginkgo leaves [84] has a larger specific surface area and a higher ID/IG ratio compared to the hard carbon derived from Tamarind fruits [83], even though they have similar d-spacing values (4.01 Å). Furthermore, the presence of inorganic impurities can vary among different biomass precursors and have a significant impact on the structure and performance of the resulting hard carbon [85]. High levels of inorganic impurities result in increased d-spacing, surface defects, and SSA. This can negatively affect sodium ion storage, leading to an increase in irreversible capacity loss in hard carbon anodes [86]. To mitigate this issue, it is crucial to remove inorganic impurities from some biomass precursors through a process such as acid washing. Thus, it is crucial to choose the right biomass precursor to achieve a high-performing hard carbon anode.

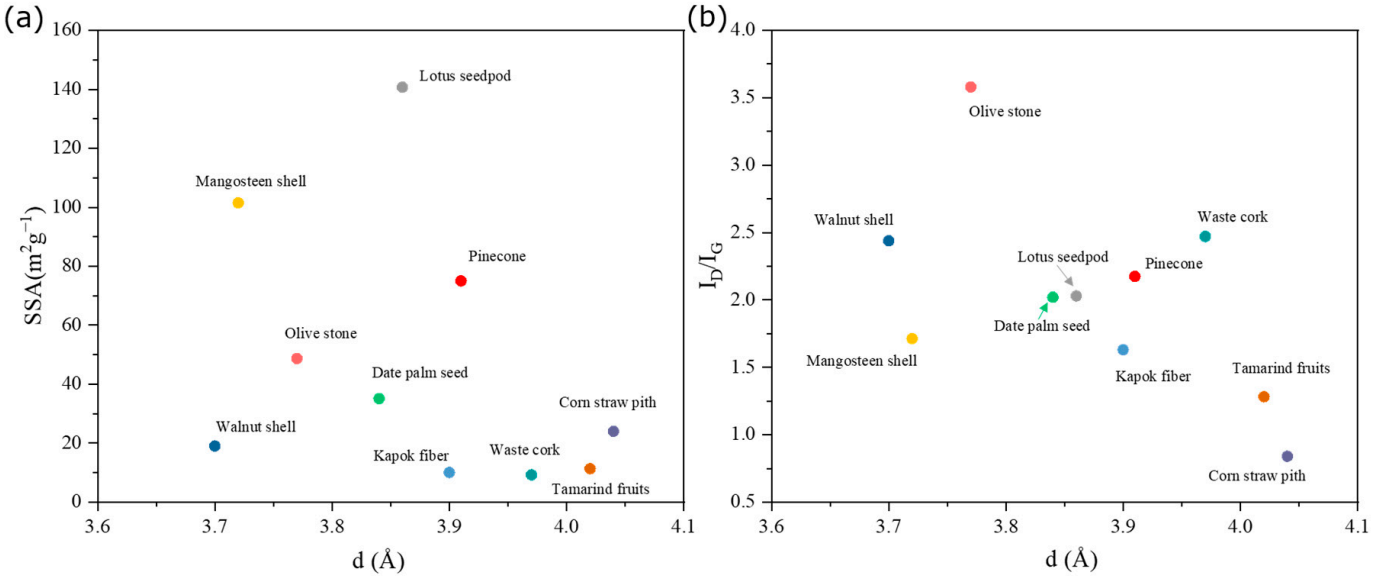


**Figure 4.** Hard carbon structure properties for different biomasses tested using the same condition (1200 °C for 2 h), including the relationship between d-spacing and (**a**) SSA, and (**b**) $I_D/I_G$. (Pinecone [56]; Mangosteen shell [57]; Lotus seedpod [58]; Waste cork [59]; Olive stone [78]; Walnut shell [79]; Kapok fiber [80]; Date palm seed [81]; Corn straw pith [82]; Tamarid fruits [83]).

### *4.2. Influence of Processing Parameters*

According to the literature, the carbonization conditions, i.e., the processing parameters of HC, have a significant effect on the structure of HC [11]. The carbonization temperature is the most studied parameter that determines the HC property. In general, the increase in the carbonization temperature causes the HC surface defects to decrease, graphite domains to grow, nanopore volume to decrease, and the structure tends to become more ordered.

To further verify the effect of carbonization temperature on the structure of HC, this review summarizes the data corresponding to the structural parameters of biomass-derived HC with carbonization temperature in recent years. The results are presented in Figure 5; the different colored dots represent different biomasses. As shown in Figure 5a, the graphene lactic layer spacing for HC graphite ranges between 4.2 and 3.6 Å. The $d_{002}$ values, which indicate the distance between graphene layers, are observed to vary among the different biomass precursors for a constant carbonization temperature. However, a common trend is observed where the $d_{002}$ value decreases with increasing carbonization temperature for all HC samples. The extent of this decrease, however, is dependent on the specific biomass precursor used. These results are also consistent with the previously reported data [87]. Figure 5b illustrates the correlation between the specific surface area (SSA) and the carbonization temperature. At low carbonization temperatures, the SSA values for HC derived from different biomass precursors span a wide range, from 0 to

1000 $m^2/g$. However, as the carbonization temperature increases, the SSA values of the HC samples converge to values below 50 $m^2/g$. This suggests that the rise in carbonization temperature effectively reduces the surface area of the HC. Figure 5c shows the relationship between the microporous volume (V) and the carbonization temperature. Although the microporous volume decreases slightly with increasing carbonization temperature, closer inspection reveals that the change in microporous volume for HC derived from different biomass precursors is not uniform. For instance, the HC derived from Ginkgo leaves [84] exhibits a fluctuation in V with rising carbonization temperature, while the HC derived from Shaddock peel [55] exhibits an increase in V with increasing temperature. Further research is required to fully understand the correlation between the microporous volume and carbonization temperature. Figure 5d,e show the relationship between the graphite domain size ($L_a$ and $L_c$) and the carbonization temperature. The size of La, which represents the size of the crystalline domains in the a-axis direction, varies between 3 and 14 nm due to the different biomass precursors. With increasing carbonization temperature, the size of La exhibits an upward trend. Similarly, Lc, the size of the crystalline domains in the c-axis direction, also shows an increase, although to a lesser extent. As the temperature rises from 800 to 1600 °C, the Lc size gradually approaches a value of 2 nm from its initial value of 1 nm, which is in agreement with previous literature [88]. These findings demonstrate that while a higher carbonization temperature promotes the growth of graphitic domains, it simultaneously decreases the d-spacing of HC. Figure 5f illustrates the relationship between the carbonization temperature and the intensity ratio of the D band to the G band ($I_D/I_G$ ratio). The $I_D/I_G$ ratio is mainly observed to range between 1.5 and 3.5. When the carbonization temperature exceeds 1500 °C, the $I_D/I_G$ ratio is found to converge to a range between 1 and 2. Specifically, the $I_D/I_G$ ratios of HC derived from Ginkgo leaves [84] and Mangosteen shells [57] decrease from 2.5 to 1.31 and 2.03 to 1.49, respectively, as the carbonization temperature increases from 800 to 1600 °C. This trend indicates that the $I_D/I_G$ ratio decreases with rising carbonization temperature, tending towards a value of approximately 1. This outcome reflects the non-graphitizable nature of HC, which retains a significant degree of disorder even at very high carbonization temperatures. In conclusion, the results suggest that as the carbonization temperature increases, the graphitic domains grow, the surface area decreases, and the graphitization degree is increased, which is in line with previous findings.

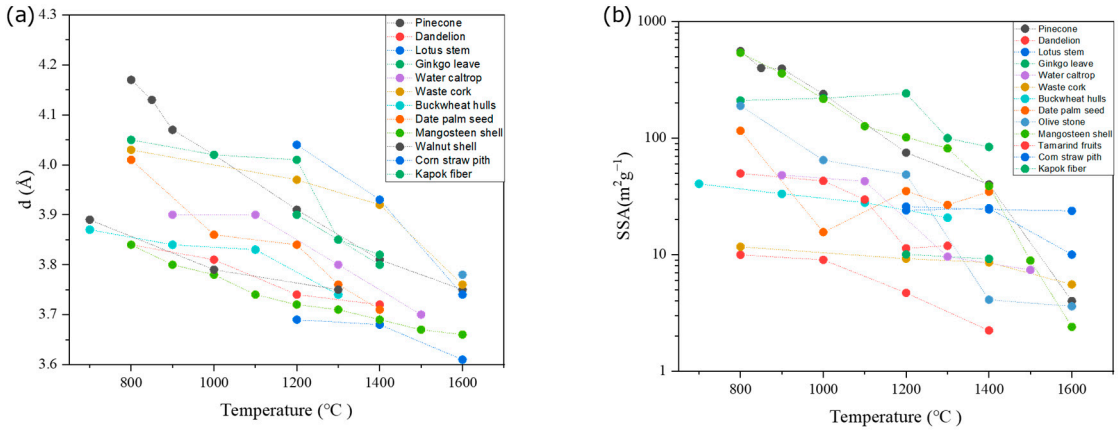


**Figure 5.** *Cont.*

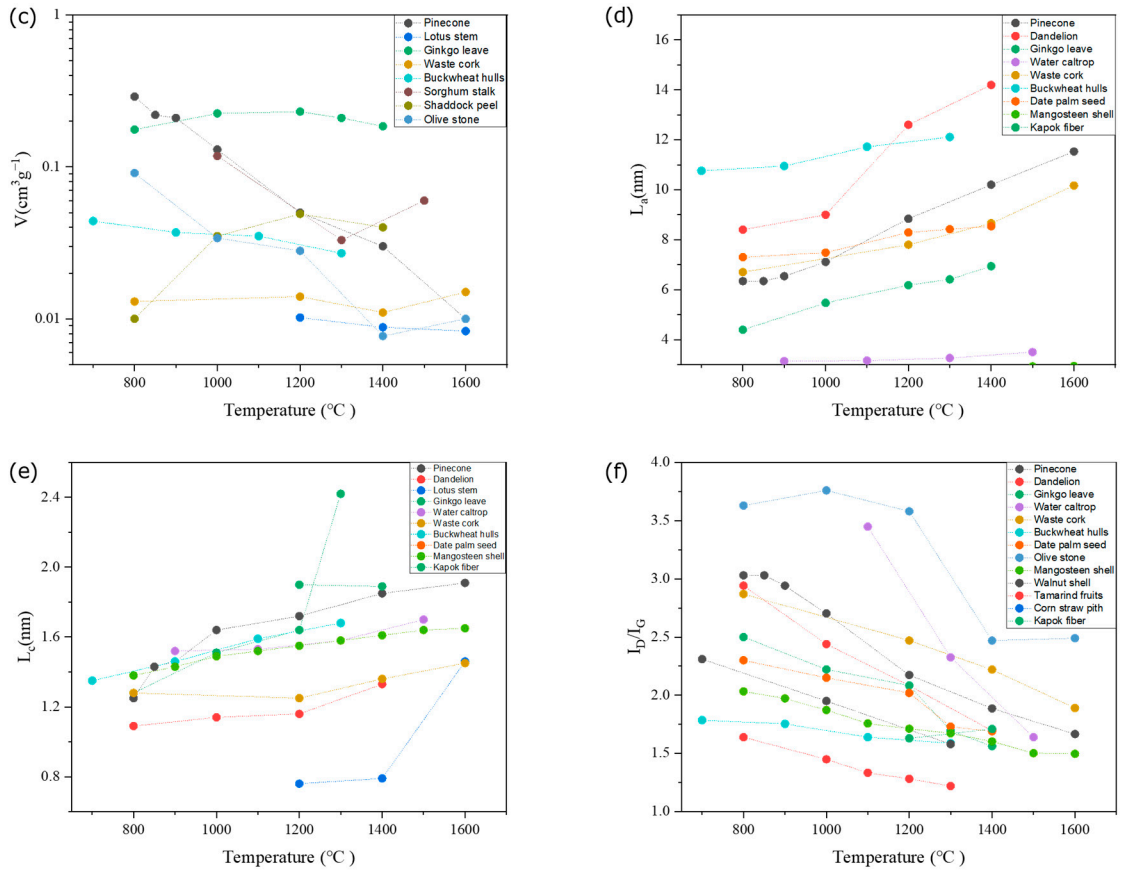


**Figure 5.** Effect of the carbonization temperature on hard carbon structure: Effect of the carbonization temperature on (**a**) $d_{002}$; (**b**) SSA; (**c**) V; (**d**) $L_a$; (**e**) $L_c$; and (**f**) $I_D/I_G$ [55,56,58,59,81,84,88–91].

## 5. Relationship between Structure and Electrochemical Performance of HCs

The HC structure is directly related to the sodium-ion storage method and contributes significantly to the electrochemical performance. The correlation between the HC structure and anode performance is summarized in Figure 6. The data are consistent with those presented in Section 4, and the electrochemical data are from half-cell tests. Four structural parameters, $d_{002}$, SSA, V, and the $I_D/I_G$ ratios, are selected to characterize the three main structures of HC: graphitic domains, surface defects, and nanopores. The main consideration is the effect of the structure on the capacity and initial Coulombic efficiency (ICE) of the HC anode.

Figure 6a illustrates the relationship between the interlayer spacing (d-spacing) and the capacity of the HC anode. The data points are mostly concentrated in the range of d-spacings from 3.6 Å to 4.0 Å, corresponding to capacities between 200 and 400 mAh/g. The data points with high capacities, greater than 320 mAh/g, are primarily located in the range of d-spacings from 3.75 to 3.95 Å. Conversely, the capacities of HC anodes decrease significantly for d-spacings greater than 4.0 Å. This suggests that the d-spacing of HC has a direct impact on the anode capacity, with the highest capacity achieved for d-spacing ranging from 3.75 to 3.95 Å. This is consistent with the findings of Au H et al. [34], who reported that d-spacing values in the range between 3.7 and 4.0 Å are most suitable for sodium ion intercalation. Values below 3.7 Å result in a high energy barrier for sodium ion intercalation, while values exceeding 4.0 Å lead to surface-like pseudo-adsorption of sodium ions instead of intercalation [11]. Figure 6b shows the relationship between the HC anode ICE and d-spacing. The data points are evenly distributed in the range of d-spacings from 3.6 to 4.05 Å, without a significant correlation trend. However, there is no established theory to support that an increase in d-spacing improves the ICE performance.

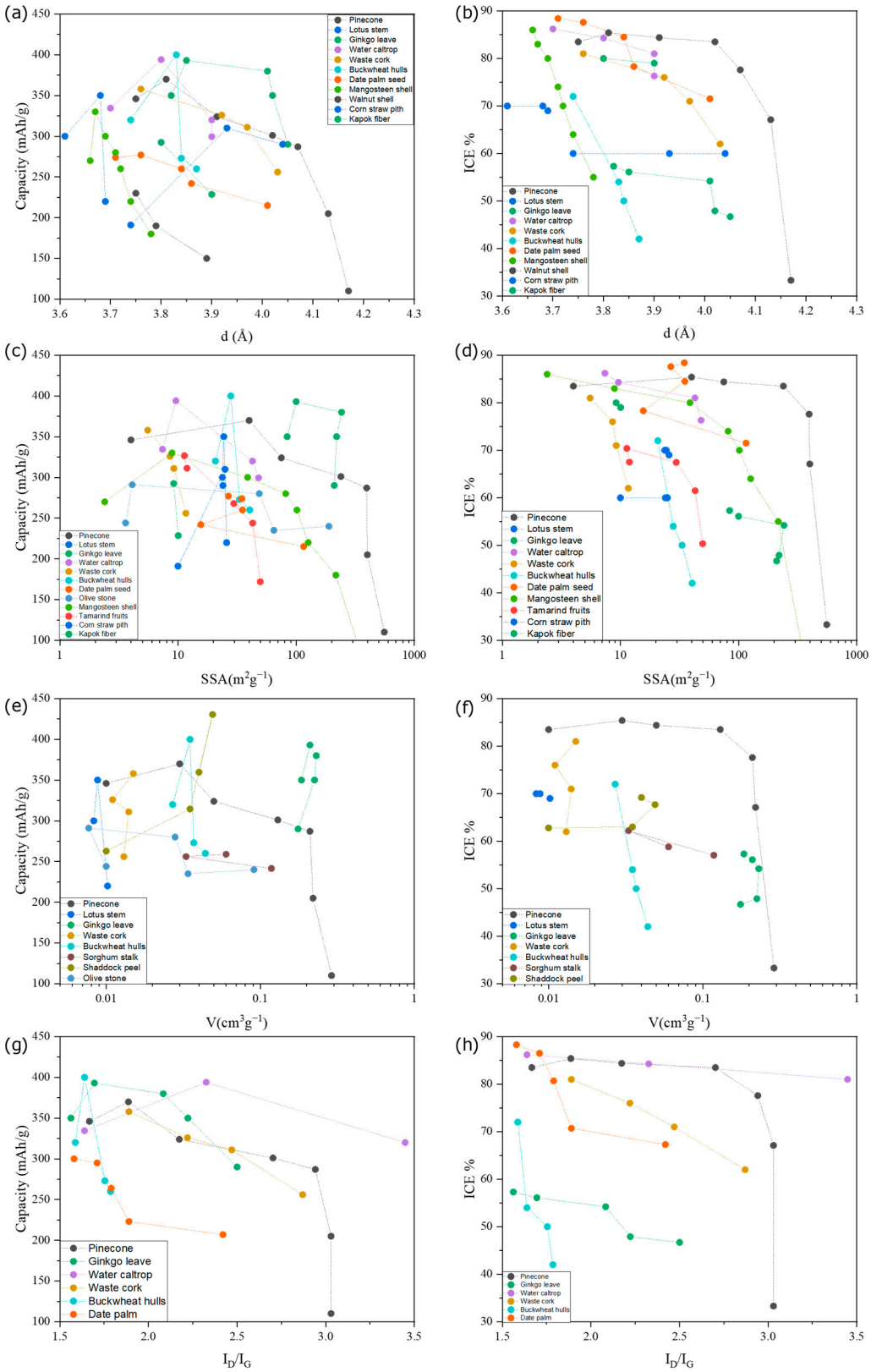


**Figure 6.** Relationship between hard carbon anode capacity and: (**a**) $d_{002;}$ (**c**) SSA; (**e**) $V_t$; (**g**) $I_D/I_G$ ratios; Relationship between hard carbon anode ICE and: (**b**) $d_{002;}$ (**d**) SSA; (**f**) $V_t$; (**h**) $I_D/I_G$ ratios [55–59,78–84,88–91].

Figure 6c reveals that the capacity of the HC anodes is evenly distributed for specific surface areas (SSA) between 0 and 200 $m^2/g$, indicating that the SSA does not have a significant influence on the anode capacity. Figure 6d shows that all HC anodes with ICE values greater than 85% have SSA values below 50 $m^2/g$. Furthermore, for the same biomass precursor, there is a noticeable increase in ICE as the SSA decreases. For instance, for HC derived from date palm [81], the ICE increases from 67% to 88% as the SSA decreases from 225 $m^2/g$ to 33 $m^2/g$. In summary, the overall distribution of data points forms a tapered pattern, with HCs exhibiting high ICE values tending to have lower SSA values, and HC with low ICE values having more variable SSA values over a wider range. This trend suggests that the SSA value directly impacts the ICE value, with lower SSA values leading to higher ICE values. This is because the higher surface area can cause irreversible sodium ion storage and the formation of a solid electrolyte interphase (SEI) layer, leading to a reduced ICE value and anode performance.

Figure 6e and f demonstrate that the relationship between the microporous volume and anode performance is not clear, as the data points are evenly distributed in the graph. Figure 6g,h shows the relationship between HC anode performance and the $I_D/I_G$ ratio. The data points with capacities greater than 300 mAh/g are mostly located in the range of $I_D/I_G$ ratios less than 2.5, while the data points with ICE values higher than 80% are mainly concentrated in the range of $I_D/I_G$ ratios lower than 2.0. However, a clear relationship between anode performance and ID/IG cannot be established. A combination of factors affects the anode capacity, and the best performance is achieved with HC structure parameters including d-spacing between 3.75 Å and 3.95 Å, $I_D/I_G$ ratios lower than 2, and SSA less than 100 $m^2/g$.

## 6. Proposed Relationship between Processing Parameters and the HC Performance

Combined with the results in Sections 4 and 5, the relationship between carbonization temperature and HC anode performance is shown in Figure 7. As the carbonization temperature increases, the capacity of the HC anode shows a parabolic trend, while the ICE shows an upward trend. This is because the increase in carbonization temperature leads to a decrease in the graphene lactic layer spacing, which is gradually suitable for sodium ion insertion The optimal range of carbonization temperature is between 1200 °C and 1400 °C, which allows for a $d_{002}$ value (3.75 Å–3.95 Å) that results in higher capacity. However, as the temperature continues to rise, the d-spacing becomes too small (less than 3.7 Å), leading to a significant increase in the energy required for sodium ion insertion, resulting in a decrease in the HC anode capacity. Additionally, according to Figure 5, high carbonization temperature causes the SSA value of HC to gradually approach a value below 50 $m^2/g$, reducing SEI layer formation sites, and thus reducing the irreversible sodium ion storage [47]. This results in a higher ICE value. The results also show different biomass precursors (different colored dots) have different optimum carbonization temperatures.

Figure 8 summarizes the relationship between the synthetic route, HC structure, and anode performance. The biomass precursors directly determine the structure of the HC. Different synthesis conditions can be used to further optimize the HC structure to achieve a better electrochemical performance. In the figure, the blue line represents the two parameter having a correlation, the red line represents a positive correlation, and the green line represents a negative correlation. It can be seen that an increased carbonization temperature will lead to reduced surface defects and SSA value, which will increase ICE. However, an excessive increase in the carbonization temperature will reduce graphite layer spacing, thus reducing the HC anode capacity. This corresponds to the trend in the data shown in Figure 7.

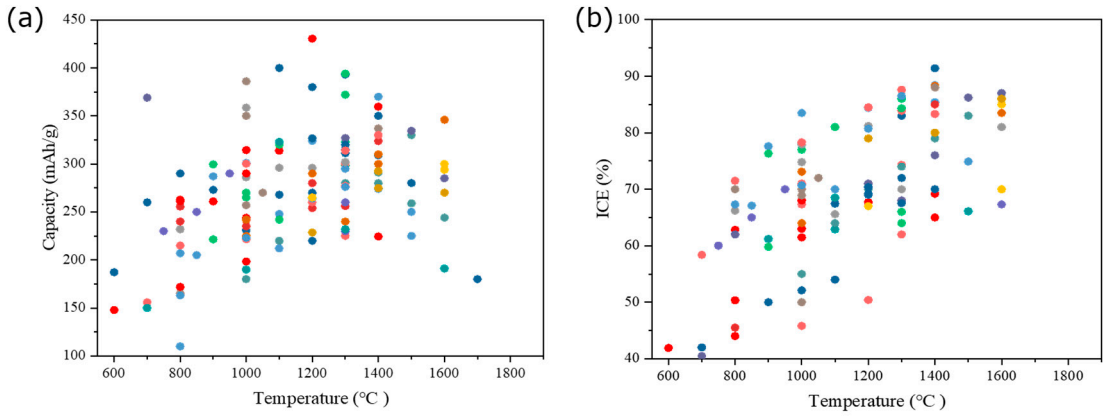


**Figure 7.** The relationship between carbonization temperature and HC anode performance: (**a**) capacity; (**b**) ICE. Different colored dots represent different biomass precursor [21,47,55–58,62,64,78,79,81–84,91–114].

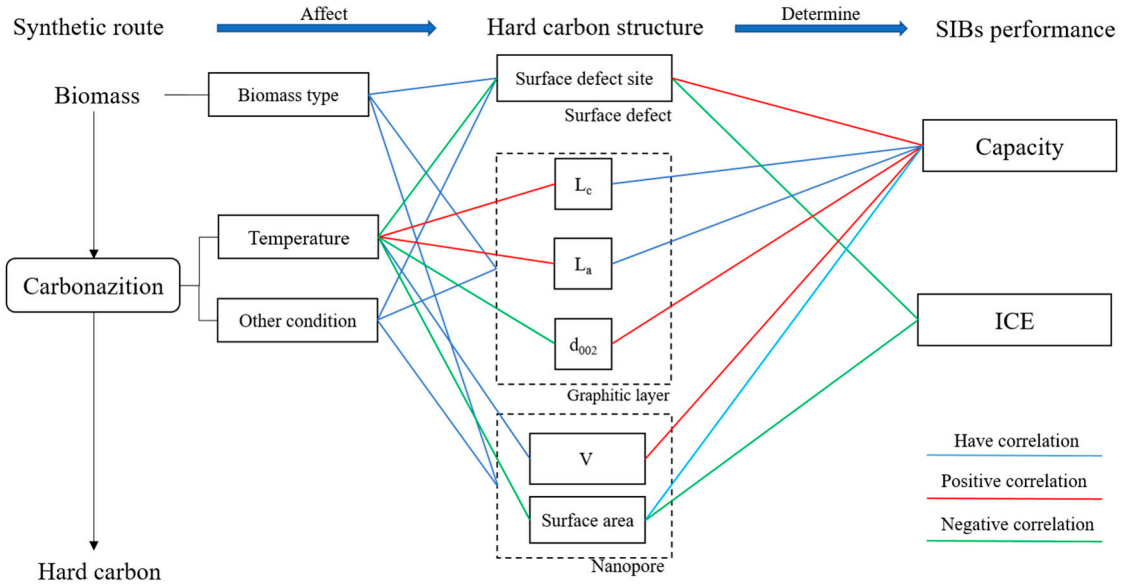


**Figure 8.** Relationship between the synthetic route, HC structure, and anode performance.

## 7. Summary and Future Outlook

The rapid expansion of the sodium ion battery market is gradually driving up demand for HC anode materials. Biomass, as a renewable, sustainable, and abundant material, is a promising precursor material to produce HCs as SIB anode materials. The selection of suitable and reliable biomass raw materials depending on geographical conditions is crucial to the manufacturing of HC. Resource abundant and industrially available HC precursor is suggested to be one of the essential points to consider in the coming HC studies.

Currently, biomass by-products originating from agroforestry and biochar originating from bio-refineries are proven to make high quality HC materials and are available in a stable supply. For example, sawdust waste from forest industries and lignin from paper industries are of interest as HC precursors. HC production as the downstream industry of the above enterprises is a very promising business model for the future. Resource efficiency of the biomass waste is also important to consider.

There is still a significant capacity gap between sodium and lithium ion batteries, mostly due to the limited capacity of HC anodes. Therefore, optimizing the HC structure to increase the capacity of HC anodes is the most important factor in enhancing the competitiveness of sodium batteries. This study reviewed the mechanism of sodium-ion

storage in HC, the biomass precursor type, processing methods and conditions of the HCs production, the effect of the biomass types and carbonization temperature on the carbon structure, and the effect of various carbon structures on electrochemical performance. In conclusion, temperature is a key factor affecting the structure of HC. As the carbonization temperature increases, the specific surface area (SSA) of HC decreases, the graphite crystals grow, the microporous volume decreases, and the structure tends to become ordered. Therefore, the selection of the optimum carbonization temperature according to the type of biomass is a central issue in HC production.

**Author Contributions:** Conceptualization, Y.J. and T.H.; methodology, Y.J. and T.H.; investigation, Y.J. and Z.S.; resources, W.Y. and R.Y.; data curation, Y.J., Z.S. and H.Y.; writing—original draft preparation, Y.J. and T.H.; writing—review and editing, P.G.J., W.Y., H.D.A. and R.G.; visualization, Y.J.; supervision, W.Y. and P.G.J. All authors have read and agreed to the published version of the manuscript.

**Funding:** This research was funded by VINNOVA with project number 2021-03735.

**Data Availability Statement:** No new data were created.

**Acknowledgments:** Financial supported by VINNOVA—the Swedish innovation Agency with project number 2021-03735 is highly appreciated.

**Conflicts of Interest:** The authors declare no conflict of interest.

## Nomenclature

| | |
|---|---|
| SIBs | sodium-ion batteries |
| LIBs | lithium-ion batteries |
| HCs | hard carbons |
| SSA | specific surface area |
| $d_{002}$ | graphene lattice layer spacing |
| ICE | initial coulombic efficiency |
| La | the crystallite width along the a-axis |
| Lc | the crystallite width along the c-axis |
| SEI | solid electrolyte interphase |

## References

1. Kim, T.; Song, W.; Son, D.-Y.; Ono, L.K.; Qi, Y. Lithium-ion batteries: Outlook on present, future, and hybridized technologies. *J. Mater. Chem. A* **2019**, *7*, 2942–2964. [CrossRef]
2. Kubota, K.; Dahbi, M.; Hosaka, T.; Kumakura, S.; Komaba, S. Towards K-ion and Na-ion batteries as "beyond Li-ion". *Chem. Rec.* **2018**, *18*, 459–479. [CrossRef]
3. Yoshino, A. The birth of the lithium-ion battery. *Angew. Chem. Int. Ed.* **2012**, *51*, 5798–5800. [CrossRef] [PubMed]
4. Yudhistira, R.; Khatiwada, D.; Sanchez, F. A comparative life cycle assessment of lithium-ion and lead-acid batteries for grid energy storage. *J. Clean. Prod.* **2022**, *358*, 131999. [CrossRef]
5. Li, M.; Lu, J.; Chen, Z.; Amine, K. 30 years of lithium-ion batteries. *Adv. Mater.* **2018**, *30*, 1800561. [CrossRef]
6. Martin, G.; Rentsch, L.; Höck, M.; Bertau, M. Lithium market research–global supply, future demand and price development. *Energy Storage Mater.* **2017**, *6*, 171–179. [CrossRef]
7. Vargas, P. Lithium and the Foreseeable Future. Bachelor's Thesis, University of Arkansas, Fayetteville, AR, USA, 2018.
8. Liu, D.; Gao, X.; An, H.; Qi, Y.; Sun, X.; Wang, Z.; Chen, Z.; An, F.; Jia, N. Supply and demand response trends of lithium resources driven by the demand of emerging renewable energy technologies in China. *Resour. Conserv. Recycl.* **2019**, *145*, 311–321. [CrossRef]
9. Chen, X.; Zheng, Y.; Liu, W.; Zhang, C.; Li, S.; Li, J. High-performance sodium-ion batteries with a hard carbon anode: Transition from the half-cell to full-cell perspective. *Nanoscale* **2019**, *11*, 22196–22205. [CrossRef]
10. Hwang, J.-Y.; Myung, S.-T.; Sun, Y.-K. Sodium-ion batteries: Present and future. *Chem. Soc. Rev.* **2017**, *46*, 3529–3614. [CrossRef]
11. Thompson, M.; Xia, Q.; Hu, Z.; Zhao, X.S. A review on biomass-derived hard carbon materials for sodium-ion batteries. *Mater. Adv.* **2021**, *2*, 5881–5905. [CrossRef]
12. Chayambuka, K.; Mulder, G.; Danilov, D.L.; Notten, P.H. Sodium-ion battery materials and electrochemical properties reviewed. *Adv. Energy Mater.* **2018**, *8*, 1800079. [CrossRef]
13. Faradion. Available online: https://faradion.co.uk/technology-benefits/strong-performance/ (accessed on 8 February 2023).
14. Natrium. Available online: http://www.natriumenergy.cn/ (accessed on 8 February 2023).

15. CATL. Available online: https://www.catl.com/ (accessed on 8 February 2023).
16. Metal price. Available online: https://www.metal.com/ (accessed on 27 February 2023).
17. Moriwake, H.; Kuwabara, A.; Fisher, C.A.; Ikuhara, Y. Why is sodium-intercalated graphite unstable? *RSC Adv.* **2017**, *7*, 36550–36554. [CrossRef]
18. Liu, Y.; Xu, Y.; Han, Y.; Zhang, Z.; Xu, J.; Du, Y.; Bao, J.; Zhou, X. Facile synthesis of SnSe2 nanoparticles supported on graphite nanosheets for improved sodium storage and hydrogen evolution. *J. Power Sources* **2019**, *436*, 226860. [CrossRef]
19. Liu, Q.; Hu, Z.; Chen, M.; Zou, C.; Jin, H.; Wang, S.; Chou, S.L.; Liu, Y.; Dou, S.X. The cathode choice for commercialization of sodium-ion batteries: Layered transition metal oxides versus Prussian blue analogs. *Adv. Funct. Mater.* **2020**, *30*, 1909530. [CrossRef]
20. Jiang, Y.; Hu, M.; Zhang, D.; Yuan, T.; Sun, W.; Xu, B.; Yan, M. Transition metal oxides for high performance sodium ion battery anodes. *Nano Energy* **2014**, *5*, 60–66. [CrossRef]
21. Zheng, Y.; Lu, Y.; Qi, X.; Wang, Y.; Mu, L.; Li, Y.; Ma, Q.; Li, J.; Hu, Y.-S. Superior electrochemical performance of sodium-ion full-cell using poplar wood derived hard carbon anode. *Energy Storage Mater.* **2019**, *18*, 269–279. [CrossRef]
22. Tin powder. Available online: https://www.alibaba.com/product-detail/Sn-Sn-Tin-Powder-Tin-Powder_62359699945.html?spm=a2700.galleryofferlist.normal_offer.d_title.23203583obX2GZ&s=p (accessed on 27 February 2023).
23. Liu, Y.; Zhang, N.; Jiao, L.; Tao, Z.; Chen, J. Ultrasmall Sn nanoparticles embedded in carbon as high-performance anode for sodium-ion batteries. *Adv. Funct. Mater.* **2015**, *25*, 214–220. [CrossRef]
24. Dong, S.; Lv, N.; Wu, Y.; Zhang, Y.; Zhu, G.; Dong, X. Titanates for sodium-ion storage. *Nano Today* **2022**, *42*, 101349. [CrossRef]
25. Zhang, Y.; Hou, H.; Yang, X.; Chen, J.; Jing, M.; Wu, Z.; Jia, X.; Ji, X. Sodium titanate cuboid as advanced anode material for sodium ion batteries. *J. Power Sources* **2016**, *305*, 200–208. [CrossRef]
26. Titanate price. Available online: https://www.sigmaaldrich.com/SE/en/search/sodium-titanate?focus=products&page=1&perpage=30&sort=relevance&term=sodium%20titanate&type=product (accessed on 27 February 2023).
27. Doeff, M.M.; Cabana, J.; Shirpour, M. Titanate anodes for sodium ion batteries. *J. Inorg. Organomet. Polym. Mater.* **2014**, *24*, 5–14. [CrossRef]
28. Xu, J.; Ding, W.; Zhao, W.; Zhao, W.; Hong, Z.; Huang, F. In situ growth enabling ideal graphene encapsulation upon mesocrystalline $MTiO_3$ (M = Ni, Co, Fe) nanorods for stable lithium storage. *ACS Energy Lett.* **2017**, *2*, 659–663. [CrossRef]
29. BTR. Available online: https://www.btrchina.com/NegativeProducts/info.aspx?itemid=822 (accessed on 27 February 2023).
30. BSG. Available online: http://www.cdbsg.com/index/news/detail.html?id=125&cid=15&pid=3 (accessed on 27 February 2023).
31. JFE. Available online: https://www.jfe-chem.com/en/product/battery/carbon/ (accessed on 27 February 2023).
32. Alvira, D.; Antorán, D.; Manyà, J.J. Plant-derived hard carbon as anode for sodium-ion batteries: A comprehensive review to guide interdisciplinary research. *Chem. Eng. J.* **2022**, *447*, 137468. [CrossRef]
33. Dou, X.; Hasa, I.; Saurel, D.; Vaalma, C.; Wu, L.; Buchholz, D.; Bresser, D.; Komaba, S.; Passerini, S. Hard carbons for sodium-ion batteries: Structure, analysis, sustainability, and electrochemistry. *Mater. Today* **2019**, *23*, 87–104. [CrossRef]
34. Au, H.; Alptekin, H.; Jensen, A.C.; Olsson, E.; O'Keefe, C.A.; Smith, T.; Crespo-Ribadeneyra, M.; Headen, T.F.; Grey, C.P.; Cai, Q. A revised mechanistic model for sodium insertion in hard carbons. *Energy Environ. Sci.* **2020**, *13*, 3469–3479. [CrossRef]
35. Asfaw, H.D.; Tai, C.-W.; Valvo, M.; Younesi, R. Facile synthesis of hard carbon microspheres from polyphenols for sodium-ion batteries: Insight into local structure and interfacial kinetics. *Mater. Today Energy* **2020**, *18*, 100505. [CrossRef]
36. Asfaw, H.D.; Gond, R.; Kotronia, A.; Tai, C.-W.; Younesi, R. Bio-derived hard carbon nanosheets with high rate sodium-ion storage characteristics. *Sustain. Mater. Technol.* **2022**, *32*, e00407. [CrossRef]
37. Chen, X.; Liu, C.; Fang, Y.; Ai, X.; Zhong, F.; Yang, H.; Cao, Y. Understanding of the sodium storage mechanism in hard carbon anodes. *Carbon Energy* **2022**, *4*, 1133–1150. [CrossRef]
38. Cheng, X.-Q.; Li, H.-J.; Zhao, Z.-X.; Wang, Y.-Z.; Wang, X.-M. The use of in-situ Raman spectroscopy in investigating carbon materials as anodes of alkali metal-ion batteries. *New Carbon Mater.* **2021**, *36*, 93–105. [CrossRef]
39. Stevens, D.; Dahn, J. High capacity anode materials for rechargeable sodium-ion batteries. *J. Electrochem. Soc.* **2000**, *147*, 1271. [CrossRef]
40. Xie, F.; Xu, Z.; Guo, Z.; Titirici, M.-M. Hard carbons for sodium-ion batteries and beyond. *Prog. Energy* **2020**, *2*, 042002. [CrossRef]
41. Moon, H.; Innocenti, A.; Liu, H.; Zhang, H.; Weil, M.; Zarrabeitia, M.; Passerini, S. Bio-waste-derived-hard carbon anodes through a sustainable and cost-effective synthesis process for Sodium-ion batteries. *ChemSusChem* **2022**, *16*, e202201713. [CrossRef] [PubMed]
42. Senthil, C.; Park, J.W.; Shaji, N.; Sim, G.S.; Lee, C.W. Biomass seaweed-derived nitrogen self-doped porous carbon anodes for sodium-ion batteries: Insights into the structure and electrochemical activity. *J. Energy Chem.* **2022**, *64*, 286–295. [CrossRef]
43. Tan, M.; Zhang, W.; Fan, C.; Li, L.; Chen, H.; Li, R.; Luo, T.; Han, S. Boric Acid–Catalyzed Hard Carbon Microfiber Derived from Cotton as a High-Performance Anode for Lithium-Ion Batteries. *Energy Technol.* **2019**, *7*, 1801164. [CrossRef]
44. Prabakar, S.R.; Han, S.C.; Park, C.; Bhairuba, I.A.; Reece, M.J.; Sohn, K.-S.; Pyo, M. Spontaneous formation of interwoven porous channels in hard-wood-based hard-carbon for high-performance anodes in potassium-ion batteries. *J. Electrochem. Soc.* **2017**, *164*, A2012. [CrossRef]
45. Lumber. Available online: https://markets.businessinsider.com/commodities/lumber-price (accessed on 24 February 2023).
46. Bagasse. Available online: https://pellets-wood.com/sell-b534_0.html (accessed on 24 February 2023).

47. Rath, P.C.; Patra, J.; Huang, H.T.; Bresser, D.; Wu, T.Y.; Chang, J.K. Carbonaceous Anodes Derived from Sugarcane Bagasse for Sodium-Ion Batteries. *ChemSusChem* **2019**, *12*, 2302–2309. [CrossRef]
48. Chen, M.; Luo, F.; Liao, Y.; Liu, C.; Xu, D.; Wang, Z.; Liu, Q.; Wang, D.; Ye, Y.; Li, S. Hard carbon derived for lignin with robust and low-potential sodium ion storage. *J. Electroanal. Chem.* **2022**, *919*, 116526. [CrossRef]
49. Lin, X.; Liu, Y.; Tan, H.; Zhang, B. Advanced lignin-derived hard carbon for Na-ion batteries and a comparison with Li and K ion storage. *Carbon* **2020**, *157*, 316–323. [CrossRef]
50. Zhang, W.; Qiu, X.; Wang, C.; Zhong, L.; Fu, F.; Zhu, J.; Zhang, Z.; Qin, Y.; Yang, D.; Xu, C.C. Lignin derived carbon materials: Current status and future trends. *Carbon Res.* **2022**, *1*, 14. [CrossRef]
51. Sawdust. Available online: https://www.alibaba.com/showroom/wood-sawdust-price.html (accessed on 24 February 2023).
52. Erdogan, V. Hazelnut production in Turkey: Current situation, problems and future prospects. In Proceedings of the IX International Congress on Hazelnut 1226, Atakum, Turkey, 15–18 August 2017; pp. 13–24.
53. Corn. Available online: https://www.statista.com/statistics/254292/global-corn-production-by-country/ (accessed on 24 February 2023).
54. Ren, J.; Yu, P.; Xu, X. Straw utilization in China—Status and recommendations. *Sustainability* **2019**, *11*, 1762. [CrossRef]
55. Sun, N.; Liu, H.; Xu, B. Facile synthesis of high performance hard carbon anode materials for sodium ion batteries. *J. Mater. Chem. A* **2015**, *3*, 20560–20566. [CrossRef]
56. Zhang, T.; Mao, J.; Liu, X.; Xuan, M.; Bi, K.; Zhang, X.L.; Hu, J.; Fan, J.; Chen, S.; Shao, G. Pinecone biomass-derived hard carbon anodes for high-performance sodium-ion batteries. *RSC Adv.* **2017**, *7*, 41504–41511. [CrossRef]
57. Wang, K.; Jin, Y.; Sun, S.; Huang, Y.; Peng, J.; Luo, J.; Zhang, Q.; Qiu, Y.; Fang, C.; Han, J. Low-cost and high-performance hard carbon anode materials for sodium-ion batteries. *ACS Omega* **2017**, *2*, 1687–1695. [CrossRef] [PubMed]
58. Zhang, N.; Liu, Q.; Chen, W.; Wan, M.; Li, X.; Wang, L.; Xue, L.; Zhang, W. High capacity hard carbon derived from lotus stem as anode for sodium ion batteries. *J. Power Sources* **2018**, *378*, 331–337. [CrossRef]
59. Li, Y.; Lu, Y.; Meng, Q.; Jensen, A.C.S.; Zhang, Q.; Zhang, Q.; Tong, Y.; Qi, Y.; Gu, L.; Titirici, M.M.; et al. Regulating pore structure of hierarchical porous waste cork-derived hard carbon anode for enhanced Na storage performance. *Adv. Energy Mater.* **2019**, *9*, 1902852. [CrossRef]
60. Wang, J.; Wang, S. Preparation, modification and environmental application of biochar: A review. *J. Clean. Prod.* **2019**, *227*, 1002–1022. [CrossRef]
61. Maity, S.K. Opportunities, recent trends and challenges of integrated biorefinery: Part I. *Renew. Sustain. Energy Rev.* **2015**, *43*, 1427–1445. [CrossRef]
62. Alvin, S.; Yoon, D.; Chandra, C.; Susanti, R.F.; Chang, W.; Ryu, C.; Kim, J. Extended flat voltage profile of hard carbon synthesized using a two-step carbonization approach as an anode in sodium ion batteries. *J. Power Sources* **2019**, *430*, 157–168. [CrossRef]
63. Biochar. Available online: https://www.alibaba.com/countrysearch/CN/biochar.html?fsb=y&IndexArea=product_en&CatId=&SearchText=biochar&isGalleryList=G (accessed on 27 February 2023).
64. Rios, C.D.M.S.; Simone, V.; Simonin, L.; Martinet, S.; Dupont, C. Biochars from various biomass types as precursors for hard carbon anodes in sodium-ion batteries. *Biomass Bioenergy* **2018**, *117*, 32–37. [CrossRef]
65. Mitchual, S.J.; Frimpong-Mensah, K.; Darkwa, N.A. Evaluation of fuel properties of six tropical hardwood timber species for briquettes. *J. Sustain. Bioenergy Syst.* **2014**, *4*, 44225. [CrossRef]
66. Miranda, N.T.; Motta, I.L.; Maciel Filho, R.; Maciel, M.R.W. Sugarcane bagasse pyrolysis: A review of operating conditions and products properties. *Renew. Sustain. Energy Rev.* **2021**, *149*, 111394. [CrossRef]
67. Grieco, E.; Baldi, G. Analysis and modelling of wood pyrolysis. *Chem. Eng. Sci.* **2011**, *66*, 650–660. [CrossRef]
68. Sørmo, E.; Silvani, L.; Thune, G.; Gerber, H.; Schmidt, H.P.; Smebye, A.B.; Cornelissen, G. Waste timber pyrolysis in a medium-scale unit: Emission budgets and biochar quality. *Sci. Total Environ.* **2020**, *718*, 137335. [CrossRef] [PubMed]
69. Garcìa-Pèrez, M.; Chaala, A.; Roy, C. Vacuum pyrolysis of sugarcane bagasse. *J. Anal. Appl. Pyrolysis* **2002**, *65*, 111–136. [CrossRef]
70. Hard carbon. Available online: https://www.alibaba.com/countrysearch/CN/hard-carbon.html (accessed on 24 February 2023).
71. Xiang, J.; Lv, W.; Mu, C.; Zhao, J.; Wang, B. Activated hard carbon from orange peel for lithium/sodium ion battery anode with long cycle life. *J. Alloys Compd.* **2017**, *701*, 870–874. [CrossRef]
72. Qi, X.; Lin, T.; Zhang, S.; Xu, J.; Zhang, H.; Xu, F.; Huang, F. Nitrogen doped hierarchical porous hard carbon derived from a facial Ti-peroxy-initiating in-situ polymerization and its application in electrochemical capacitors. *Microporous Mesoporous Mater.* **2020**, *294*, 109884. [CrossRef]
73. Li, Z.; Bommier, C.; Chong, Z.S.; Jian, Z.; Surta, T.W.; Wang, X.; Xing, Z.; Neuefeind, J.C.; Stickle, W.F.; Dolgos, M. Mechanism of Na-ion storage in hard carbon anodes revealed by heteroatom doping. *Adv. Energy Mater.* **2017**, *7*, 1602894. [CrossRef]
74. Dewar, D.; Glushenkov, A.M. Optimisation of sodium-based energy storage cells using pre-sodiation: A perspective on the emerging field. *Energy Environ. Sci.* **2021**, *14*, 1380–1401. [CrossRef]
75. Qi, H.; Xu, J.; Sun, P.; Qi, X.; Xiao, Y.; Zhao, W.; Joshi, R.; Huang, F. Tailoring Conductive 3D Porous Hard Carbon for Supercapacitors. *Energy Technol.* **2022**, *10*, 2101103. [CrossRef]
76. Antar, M.; Lyu, D.; Nazari, M.; Shah, A.; Zhou, X.; Smith, D.L. Biomass for a sustainable bioeconomy: An overview of world biomass production and utilization. *Renew. Sustain. Energy Rev.* **2021**, *139*, 110691. [CrossRef]
77. Vassilev, S.V.; Baxter, D.; Andersen, L.K.; Vassileva, C.G.; Morgan, T.J. An overview of the organic and inorganic phase composition of biomass. *Fuel* **2012**, *94*, 1–33. [CrossRef]

78. Gomez-Martin, A.; Martinez-Fernandez, J.; Ruttert, M.; Winter, M.; Placke, T.; Ramirez-Rico, J. Correlation of structure and performance of hard carbons as anodes for sodium ion batteries. *Chem. Mater.* **2019**, *31*, 7288–7299. [CrossRef]
79. Zhang, S.; Li, Y.; Li, M. Porous hard carbon derived from walnut shell as an anode material for sodium-ion batteries. *JOM* **2018**, *70*, 1387–1391. [CrossRef]
80. Yu, Z.-E.; Lyu, Y.; Wang, Y.; Xu, S.; Cheng, H.; Mu, X.; Chu, J.; Chen, R.; Liu, Y.; Guo, B. Hard carbon micro-nano tubes derived from kapok fiber as anode materials for sodium-ion batteries and the sodium-ion storage mechanism. *Chem. Commun.* **2020**, *56*, 778–781. [CrossRef]
81. Izanzar, I.; Dahbi, M.; Kiso, M.; Doubaji, S.; Komaba, S.; Saadoune, I. Hard carbons issued from date palm as efficient anode materials for sodium-ion batteries. *Carbon* **2018**, *137*, 165–173. [CrossRef]
82. Zhu, Y.-E.; Gu, H.; Chen, Y.-N.; Yang, D.; Wei, J.; Zhou, Z. Hard carbon derived from corn straw piths as anode materials for sodium ion batteries. *Ionics* **2018**, *24*, 1075–1081. [CrossRef]
83. Yu, K.; Zhao, H.; Wang, X.; Zhang, M.; Dong, R.; Li, Y.; Bai, Y.; Xu, H.; Wu, C. Hyperaccumulation route to Ca-rich hard carbon materials with cation self-incorporation and interlayer spacing optimization for high-performance sodium-ion batteries. *ACS Appl. Mater. Interfaces* **2020**, *12*, 10544–10553. [CrossRef] [PubMed]
84. Sun, N.; Guan, Z.; Liu, Y.; Cao, Y.; Zhu, Q.; Liu, H.; Wang, Z.; Zhang, P.; Xu, B. Extended "Adsorption–Insertion" Model: A New Insight into the Sodium Storage Mechanism of Hard Carbons. *Adv. Energy Mater.* **2019**, *9*, 1901351. [CrossRef]
85. Ghimbeu, C.M.; Zhang, B.; de Yuso, A.M.; Réty, B.; Tarascon, J.-M. Valorizing low cost and renewable lignin as hard carbon for Na-ion batteries: Impact of lignin grade. *Carbon* **2019**, *153*, 634–647. [CrossRef]
86. Beda, A.; Le Meins, J.-M.; Taberna, P.-L.; Simon, P.; Ghimbeu, C.M. Impact of biomass inorganic impurities on hard carbon properties and performance in Na-ion batteries. *Sustain. Mater. Technol.* **2020**, *26*, e00227. [CrossRef]
87. Alvin, S.; Yoon, D.; Chandra, C.; Cahyadi, H.S.; Park, J.-H.; Chang, W.; Chung, K.Y.; Kim, J. Revealing sodium ion storage mechanism in hard carbon. *Carbon* **2019**, *145*, 67–81. [CrossRef]
88. Yu, P.; Tang, W.; Wu, F.-F.; Zhang, C.; Luo, H.-Y.; Liu, H.; Wang, Z.-G. Recent progress in plant-derived hard carbon anode materials for sodium-ion batteries: A review. *Rare Met.* **2020**, *39*, 1019–1033. [CrossRef]
89. Wang, P.; Fan, L.; Yan, L.; Shi, Z. Low-cost water caltrop shell-derived hard carbons with high initial coulombic efficiency for sodium-ion battery anodes. *J. Alloys Compd.* **2019**, *775*, 1028–1035. [CrossRef]
90. Chen, C.; Huang, Y.; Zhu, Y.; Zhang, Z.; Guang, Z.; Meng, Z.; Liu, P. Nonignorable influence of oxygen in hard carbon for sodium ion storage. *ACS Sustain. Chem. Eng.* **2020**, *8*, 1497–1506. [CrossRef]
91. Wang, C.; Huang, J.; Qi, H.; Cao, L.; Xu, Z.; Cheng, Y.; Zhao, X.; Li, J. Controlling pseudographtic domain dimension of dandelion derived biomass carbon for excellent sodium-ion storage. *J. Power Sources* **2017**, *358*, 85–92. [CrossRef]
92. Luo, W.; Shen, F.; Clement, B. Ultra-thick, low-tortuosity, and mesoporous wood carbon anode for high-performance sodium-ion batteries. *ACC Chem. Res.* **2016**, *49*, 231. [CrossRef] [PubMed]
93. Li, H.; Shen, F.; Luo, W.; Dai, J.; Han, X.; Chen, Y.; Yao, Y.; Zhu, H.; Fu, K.; Hitz, E. Carbonized-leaf membrane with anisotropic surfaces for sodium-ion battery. *ACS Appl. Mater. Interfaces* **2016**, *8*, 2204–2210. [CrossRef]
94. Liu, P.; Li, Y.; Hu, Y.-S.; Li, H.; Chen, L.; Huang, X. A waste biomass derived hard carbon as a high-performance anode material for sodium-ion batteries. *J. Mater. Chem. A* **2016**, *4*, 13046–13052. [CrossRef]
95. Kim, K.; Lim, D.G.; Han, C.W.; Osswald, S.; Ortalan, V.; Youngblood, J.P.; Pol, V.G. Tailored carbon anodes derived from biomass for sodium-ion storage. *ACS Sustain. Chem. Eng.* **2017**, *5*, 8720–8728. [CrossRef]
96. Dahbi, M.; Kiso, M.; Kubota, K.; Horiba, T.; Chafik, T.; Hida, K.; Matsuyama, T.; Komaba, S. Synthesis of hard carbon from argan shells for Na-ion batteries. *J. Mater. Chem. A* **2017**, *5*, 9917–9928. [CrossRef]
97. Zhang, F.; Yao, Y.; Wan, J.; Henderson, D.; Zhang, X.; Hu, L. High temperature carbonized grass as a high performance sodium ion battery anode. *ACS Appl. Mater. Interfaces* **2017**, *9*, 391–397. [CrossRef]
98. Gaddam, R.R.; Jiang, E.; Amiralian, N.; Annamalai, P.K.; Martin, D.J.; Kumar, N.A.; Zhao, X. Spinifex nanocellulose derived hard carbon anodes for high-performance sodium-ion batteries. *Sustain. Energy Fuels* **2017**, *1*, 1090–1097. [CrossRef]
99. Wang, P.; Zhu, X.; Wang, Q.; Xu, X.; Zhou, X.; Bao, J. Kelp-derived hard carbons as advanced anode materials for sodium-ion batteries. *J. Mater. Chem. A* **2017**, *5*, 5761–5769. [CrossRef]
100. Zhu, X.; Jiang, X.; Liu, X.; Xiao, L.; Cao, Y. A green route to synthesize low-cost and high-performance hard carbon as promising sodium-ion battery anodes from sorghum stalk waste. *Green Energy Environ.* **2017**, *2*, 310–315. [CrossRef]
101. Puthusseri, D.; Ogale, S.; Kumar, A.; Shelke, M.V.; Gawli, Y.; Wahid, M. Nutty Carbon: Morphology Replicating Hard Carbon from Walnut Shell for Na Ion Battery Anode. *ACS Omega* **2017**, *2*, 3601–3609.
102. Wang, Y.; Feng, Z.; Zhu, W.; Gariépy, V.; Gagnon, C.; Provencher, M.; Laul, D.; Veillette, R.; Trudeau, M.L.; Guerfi, A. High capacity and high efficiency maple tree-biomass-derived hard carbon as an anode material for sodium-ion batteries. *Materials* **2018**, *11*, 1294. [CrossRef] [PubMed]
103. Zheng, Y.; Wang, Y.; Lu, Y.; Hu, Y.-S.; Li, J. A high-performance sodium-ion battery enhanced by macadamia shell derived hard carbon anode. *Nano Energy* **2017**, *39*, 489–498. [CrossRef]
104. Dou, X.; Geng, C.; Buchholz, D.; Passerini, S. Research Update: Hard carbon with closed pores from pectin-free apple pomace waste for Na-ion batteries. *APL Mater.* **2018**, *6*, 047501. [CrossRef]
105. Zhang, Y.; Li, X.; Dong, P.; Wu, G.; Xiao, J.; Zeng, X.; Zhang, Y.; Sun, X. Honeycomb-like hard carbon derived from pine pollen as high-performance anode material for sodium-ion batteries. *ACS Appl. Mater. Interfaces* **2018**, *10*, 42796–42803. [CrossRef]

106. Wang, Q.; Zhu, X.; Liu, Y.; Fang, Y.; Zhou, X.; Bao, J. Rice husk-derived hard carbons as high-performance anode materials for sodium-ion batteries. *Carbon* **2018**, *127*, 658–666. [CrossRef]
107. Zhu, Z.; Liang, F.; Zhou, Z.; Zeng, X.; Wang, D.; Dong, P.; Zhao, J.; Sun, S.; Zhang, Y.; Li, X. Expanded biomass-derived hard carbon with ultra-stable performance in sodium-ion batteries. *J. Mater. Chem. A* **2018**, *6*, 1513–1522. [CrossRef]
108. Wu, F.; Liu, L.; Yuan, Y.; Li, Y.; Bai, Y.; Li, T.; Lu, J.; Wu, C. Expanding interlayer spacing of hard carbon by natural K+ doping to boost Na-ion storage. *ACS Appl. Mater. Interfaces* **2018**, *10*, 27030–27038. [CrossRef] [PubMed]
109. Rybarczyk, M.K.; Li, Y.; Qiao, M.; Hu, Y.-S.; Titirici, M.-M.; Lieder, M. Hard carbon derived from rice husk as low cost negative electrodes in Na-ion batteries. *J. Energy Chem.* **2019**, *29*, 17–22. [CrossRef]
110. Panda, M.R.; Dutta, D.P.; Mitra, S. Bio-derived mesoporous disordered carbon: An excellent anode in sodium-ion battery and full-cell lab prototype. *Carbon* **2019**, *143*, 402–412.
111. Wu, F.; Zhang, M.; Bai, Y.; Wang, X.; Dong, R.; Wu, C. Lotus seedpod-derived hard carbon with hierarchical porous structure as stable anode for sodium-ion batteries. *ACS Appl. Mater. Interfaces* **2019**, *11*, 12554–12561. [CrossRef] [PubMed]
112. Lu, M.; Huang, Y.; Chen, C. Cedarwood Bark-derived hard carbon as an anode for high-performance sodium-ion batteries. *Energy Fuels* **2020**, *34*, 11489–11497. [CrossRef]
113. Nakabayashi, K.; Yi, H.; Ryu, D.-Y.; Chung, D.; Miyawaki, J.; Yoon, S.-H. Enhancement of first cycle coulombic efficiency of hard carbon derived from eucalyptus in a sodium ion battery. *Chem. Lett.* **2019**, *48*, 753–755. [CrossRef]
114. Marino, C.; Cabanero, J.; Povia, M.; Villevieille, C. Biowaste lignin-based carbonaceous materials as anodes for Na-ion batteries. *J. Electrochem. Soc.* **2018**, *165*, A1400. [CrossRef]